hydrogen

MDPI

Article

Optimizing In-Cylinder Charge Preparation in H2DI IC Engines: The Impact of Nozzle Cap Azimuthal and Inclination Angles on Jet Breakup

Brijesh Kinkhabwala *, Koushal Krishna, Uwe Wagner and Thomas Koch

Institute of Internal Combustion Engines (IFKM), Karlsruhe Institute of Technology (KIT), 76131 Karlsruhe, Germany
* Correspondence: brijesh.kinkhabwala@kit.edu

Abstract

In recent years, hydrogen-fueled internal combustion engines offer significant potential for achieving high efficiency and near-zero carbon emissions. However, stable combustion remains challenging due to the limited time available for fuel–air mixing, particularly in direct-injection concepts. This study investigates the influence of injector orientation on in-cylinder charge preparation in a heavy-duty spark-ignition engine operating with a side-mounted hydrogen direct-injection strategy. Three-dimensional computational fluid dynamics (CFD) simulations are performed to evaluate the effects of injector blow-cap inclination and azimuthal alignment on hydrogen jet evolution, flow-field development, and mixture formation. Under high-pressure injection conditions, hydrogen enters the cylinder as a highly under-expanded jet with strong momentum, resulting in significant interaction with the in-cylinder flow field. The results show that injector inclination influences jet impingement behavior, wall-guided flow development, and subsequent vortex evolution, while injector rotation modifies the interaction between the jet trajectory and in-cylinder swirl motion, affecting aerodynamic shear and flow-field complexity. The resulting mixture formation is evaluated through local air–fuel ratio distribution together with flow-field analysis and streamline evolution, demonstrating strong sensitivity to injector orientation and its coupling with in-cylinder aerodynamic structures. Quantitatively, injector orientation produces significant changes in the local air–fuel ratio distribution, with up to 25% reduction in the standard deviation of local air–fuel ratio for inclination variations and up to 35% for azimuthal variations between the extreme configurations, indicating improved mixture uniformity. Configurations promoting earlier jet disruption and enhanced spatial dispersion achieve more homogeneous charge preparation, whereas stronger wall-guided jet attachment results in localized fuel-rich regions. The findings provide physical insight into the role of jet–wall interaction, aerodynamic shear, and vortex restructuring in governing hydrogen mixing processes. The simulation framework captures the relevant in-cylinder flow physics and provides trends consistent with available experimental observations in the literature, which report improved efficiency and reduced NOx emissions under enhanced mixture homogeneity conditions.

Keywords: hydrogen direct injection; mixture homogeneity; under-expanded jet; nozzle cap geometry; side-injection; computational fluid dynamics (CFD)

Academic Editors: Hongjun Fan and Peggy Chen

Received: 25 June 2026
Revised: 17 August 2026
Accepted: 18 August 2026
Published: 21 August 2026

1. Introduction

Stringent environmental regulations, driven by global concerns over pollution and greenhouse gas (GHG) emissions, have catalyzed a fundamental shift toward clean energy portfolios. A primary example is the European Green Deal [1] which establishes a framework for achieving climate neutrality by 2050. Within this landscape, road transportation is a critical target, as it is responsible for approximately 70% of the sector's total emissions [2]. Consequently, there is an urgent demand for technological breakthroughs to drive rapid decarbonization. While battery electric vehicles (BEVs) are widely endorsed by legislation as a "zero-emission" solution [3], their full-scale adoption faces significant hurdles, including limited driving range, underdeveloped charging infrastructure, and the high environmental costs associated with mining rare earth metals [4]. Furthermore, the true carbon intensity of BEVs is not zero when considering the entire life cycle and the current reliance on non-renewable electricity generation [5,6]. Given these challenges, the development of zero-emission propulsion based on established technologies is becoming increasingly strategic. Hydrogen emerges as a particularly promising energy carrier due to its potential for zero carbon monoxide and carbon dioxide emissions at the point of use [7]. Hydrogen internal combustion engines (H2 ICE) offer a robust and viable solution, especially for heavy-duty and high-performance sectors that are difficult to electrify [8]. Unlike fuel cell electric vehicles (FCEVs), which require expensive precious metals and complex cooling systems, H2-ICEs leverage well-consolidated engine technology and existing manufacturing infrastructure, significantly reducing transitional costs [9]. Hydrogen's unique properties, such as a wide flammability range [10] and high laminar flame speed [11], allow for ultra-lean operation, which enhances thermal efficiency [12,13] (brake thermal efficiencies exceeding 45%) [14] while mitigating nitrogen oxide (NOx) emissions. Thus, H2-ICEs represent a critical technological enabler for achieving carbon neutrality while satisfying both regulatory requirements and market demands for performance and reliability. However, hydrogen's low ignition energy and high reactivity also introduce risks of backfire and pre-ignition, particularly in port-fuel-injected (PFI) configurations [15,16]. Direct injection (DI) has emerged as a robust solution to alleviate these combustion anomalies by completely eliminating fuel from the intake manifold and enabling localized control over charge stratification. However, transitioning to an H2 DI architecture introduces its own set of critical challenges, primarily centered around the extremely compressed timescales available for fuel–air mixing within the engine cycle. To overcome these performance and emission hurdles, researchers must optimize the primary driver of direct-injection mixture formation: the high-pressure injected jet.

Previous studies [17] have shown that controlling localized turbulence intensity can enhance flame propagation, stabilize lean combustion, and reduce NOx emissions through improved mixing and temperature distribution. Similarly, it has been reported [18] that localized fuel-rich regions, resulting from delayed injection and poor mixture preparation, can lead to severe knock under lean-burn direct-injection spark-ignition conditions. In addition, investigations [19] indicate that the orientation of the injected fuel relative to in-cylinder geometry strongly influences flow development, determining whether efficient mixing is achieved or fuel becomes trapped within unfavourable vortex structures. Despite these insights, current research typically treats in-cylinder turbulence as a pre-existing baseline or examines its downstream effects on flame propagation, leaving a critical gap in the literature. Very few studies have investigated the foundational mechanics of how this turbulence is physically generated in the first place, or how the massive influx of kinetic energy carried by the under-expanded supersonic jet is responsible for reshaping the entire fluid dynamic environment. Moreover, there is a lack of deep understanding regarding how foundational hardware-based baseline geometries, such as injection and blow cap angles, reshape pre-existing turbulence in heavy-duty engines. This work directly addresses these research gaps by evaluating a three-dimensional CAD model of a heavy-duty, single-cylinder research engine utilizing a lateral spark-ignition H2 DI strategy. The numerical framework isolates the foundational source of in-cylinder turbulence by mapping how the supersonic jet evolves and aerodynamically interacts with the pre-existing flow field. These complex fluid dynamic interactions are systematically tailored through physical geometric adjustments to the multi-hole nozzle cap's azimuthal and inclination angles. By decoupling the influence of these hardware constraints from transient electronic control calibrations, the investigation establishes clear design guidelines to optimize charge preparation in hydrogen-fueled propulsion systems.

2. Simulation Setup

2.1. CAD Architecture and Case Study

The present investigation is based on a three-dimensional CAD model of a heavy-duty, single-cylinder research engine designed for spark-ignition hydrogen direct injection (SI H_2-DI). To ensure that the simulation results remain representative of industry-relevant engine configurations, the primary geometric features—including the intake and exhaust port profiles—were fully resolved during the gas exchange phase. The fundamental engine specifications and initial wall temperature conditions are summarized in Table 1. The intake and exhaust boundary conditions were derived from experimental measurements, where high-frequency pressure data were recorded and subsequently processed using a one-dimensional GT-Power model. This approach enabled minor corrections to boundary conditions and accurate estimation of thermodynamic states. The mean values of intake and exhaust pressure and temperature were extracted and applied in the CFD simulations, as reported in Table 2. Wall temperature conditions were adopted from a validated baseline CFD model of the base engine and maintained consistently within the GT-Power model. This ensured proper calibration of cylinder filling and compression characteristics across both the 1D and 3D simulation frameworks.

Table 1. Main specifications of the simulated H2-DI engine and initial wall temperatures.

Parameter	Value
Displacement [cc]	1283
Bore [mm]	110
Stroke [mm]	135
Compression Ratio	13.4:1
Rel. air fuel ratio	2.5
Number of Valves	4
Piston Bowl Type	Hemispherical
Engine Speed [rpm]	1600
IMEP [bar]	14

The simulations were conducted at high engine speed (1600 rpm) to reflect the challenges associated with limited injection duration, which significantly affects mixture homogeneity in hydrogen direct injection systems. The cylinder head architecture incorporates a centrally positioned spark plug and a four-valve configuration, imposing strict geometric constraints. In practical engine designs, a centrally located injector would require a structurally weak bridge between valve seats, compromising both thermal management and mechanical integrity. To replicate realistic engineering constraints, a lateral injection strategy was adopted. As illustrated in Figure 1, the injector is positioned on the periphery of the combustion chamber, between the intake and exhaust valves. An outward-opening gaseous injector with a maximum injection pressure of 20 bar is employed. High injection

https://doi.org/10.3390/hydrogen7030123

pressure is essential because fuel delivery occurs during the compression stroke, requiring a pressure ratio sufficiently higher than in-cylinder pressure to ensure continuous and stable injection. Maintaining a high-pressure differential minimizes the influence of in-cylinder flow fluctuations on the injection process.

Table 2. Boundary condition and initialization.

Parameter	Value
Intake Pressure [bar]	3.1
Intake Temperature [K]	310
Exhaust Temperature [K]	700
Exhaust Pressure [bar]	3.05
Piston Bowl Temperature [K]	526
Cylinder Head Temperature [K]	556
Cylinder Liner Temperature [K]	473
Intake Valve Temperature [K]	490
Exhaust Valve Temperature [K]	723

(**a**)

(**b**)

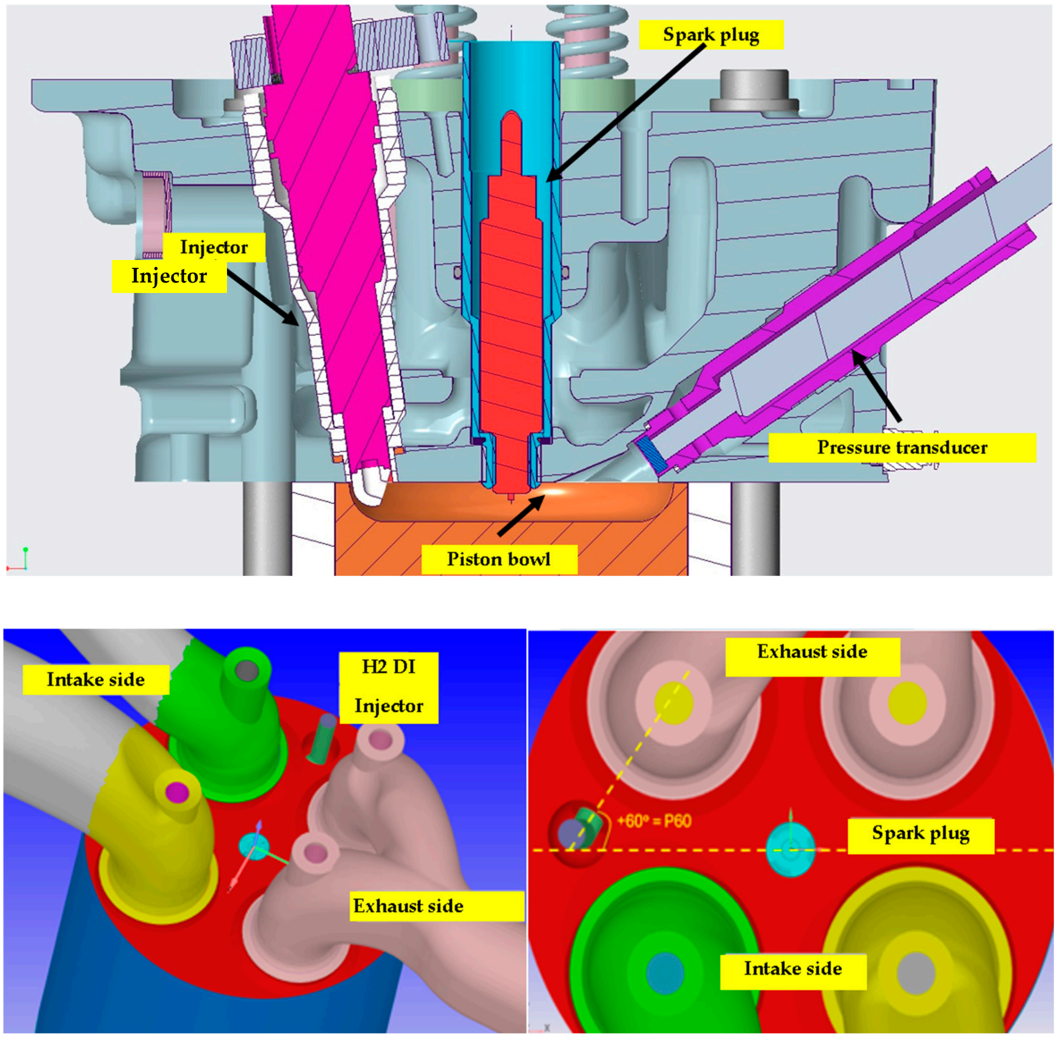

Figure 1. (**a**) Longitudinal cross-section of the cylinder assembly highlighting the internal architecture and piston bowl; (**b**) Perspective and plan views detailing the lateral injector orientation and valve-train spatial constraints.

Furthermore, the injector orientation is designed to interact constructively with the in-cylinder flow field. By inclining the injector relative to the intake-generated tumble and swirl motions, the momentum of the hydrogen jet enhances large-scale transport and promotes improved air–fuel mixing throughout the combustion chamber.

2.2. Computational Framework

Three-dimensional CFD simulations were performed using CONVERGE CFD (version 4.1). The governing Reynolds-Averaged Navier–Stokes (RANS) equations were solved using a density-based PISO scheme, with pressure–velocity coupling handled via a generalized Rhie–Chow interpolation. Turbulence closure was achieved using the Renormalization Group (RNG) k–ε model (Han and Reitz formulation), selected for its robustness in capturing jet-induced turbulence in high-speed, compressible flows [20], using Rapid Distortion RNG k-e model uses with standard models constants ($C\mu = 0.0845$, $C\varepsilon1 = 1.42$, $C\varepsilon2 = 1.68$, $C\varepsilon3 = -1.0$) and standard wall functions. No turbulent Mach-number-based dilatational-dissipation or density-gradient correction was activated; the $C\varepsilon3$ term accounts only for mean dilatation effects (e.g., local compression/expansion) rather than supersonic compressibility corrections. The numerical methodology employed in this study is summarized in Table 3. Convective fluxes of momentum, density, and energy were discretized using a second-order central flux-blending scheme. In contrast, the transport equations for turbulent kinetic energy (k) and its dissipation rate (ε) were solved using a first-order upwind scheme to ensure numerical stability. All discretization schemes were combined with a STEP flux limiter (tolerance = 0.025). This hybrid approach provides a balance between accuracy and stability: higher-order schemes improve resolution in smooth flow regions, while the added numerical dissipation from the upwind scheme suppresses non-physical oscillations near shocks and strong gradients. A refined computational grid was employed in the injector region to accurately capture steep gradients in velocity, density, and species concentration. Numerical diffusion was further minimized through Adaptive Mesh Refinement (AMR), dynamically triggered by local gradients of velocity (0.1 m/s), temperature (2.5 K), and species mass fraction (1×10^{-4}), achieving a minimum cell size of 0.125 mm in critical regions such as the jet shear layer and shock fronts. The mesh settings, including AMR criteria and minimum cell size, a dedicated case-specific mesh independence study was not performed for the present configuration due to computational resource constraints were adopted from prior verification studies in the literature [21]. Temporal resolution was maintained using a variable time-step scheme with a minimum time step of 1×10^{-8} s, with stability and accuracy enforced through Courant–Friedrichs–Lewy (CFL) limits of 1.0 for convection, 2.0 for diffusion, and 50.0 for Mach-number-based constraints [21].

Table 3. Numerical methods and models employed during simulations.

Parameter	Model
Solver	Density-based PISO Scheme
Numerical discretisation Scheme	Finite-volume
Temporal discretisation	Transient Solver (first-order implicit Euler)
Turbulence model	RNG k-epsilon
Pressure–velocity coupling	Generalized Rhie-Chow scheme, Second-order central scheme for Gradient, Second-order central scheme for density, Second-order central scheme for Momentum,
Spatial discretisation	Second-order central scheme for Energy, First-order upwind scheme for K and Epsilon

The injector model and operating conditions were consistent with those used in the reference study [22,23] allowing direct comparison for validation purposes. Experimental Background-Oriented Schlieren (BOS) data were used for validation. As BOS offers sufficient accuracy for macroscopic jet characterization but limited spatial resolution for resolving fine shock-cell structure, the present validation is restricted to jet penetration length (quantitative) and overall plume/Mach disk morphology (qualitative only); no quantitative validation of Mach disk location or barrel-shock structure is claimed.

Wall temperatures (Table 2) were derived from a baseline diesel engine simulation model, refined through 1D GT-Power simulations to match target volumetric efficiency, and further adjusted over two to three iterations in the 3D CFD model for 1D–3D consistency. This wall-temperature methodology was previously validated in a separate study by the authors involving hot-spot localization, where predicted in-cylinder pressure and heat release rate profiles matched experimental data [24]. A dedicated sensitivity analysis using lower/higher wall-temperature conditions was not performed in the present study and is identified as a direction for future work, given the expected influence of wall temperature on hydrogen density, jet penetration, wall interaction, and equivalence-ratio distribution. Heat transfer was modeled using the O'Rourke and Amsden model, which has an established track record modelling thermal exchange across diverse combustion regimes, from conventional spark-ignition [22] and pre-chamber architectures [25] to non-premixed compression-ignition engines. Hydrogen injection was treated as a gaseous inflow, with instantaneous mass flow rate determined from upstream pressure conditions and nozzle geometry.

Boundary conditions included mass flow at the injector inlet, initial thermodynamic conditions within the cylinder (mapped from a full-cycle simulation at intake valve closing), and no-slip walls with fixed temperatures. Thermophysical properties of hydrogen were obtained using the built-in CONVERGE C3 mechanism. The analysis of hydrogen jet behavior was divided into two regions: a near-field region, focusing on shock structure formation and early jet dynamics, and a far-field region, emphasizing macroscopic jet characteristics such as penetration, cone angle, and mixing behavior.

2.3. Simulation Validation

The numerical model was validated against experimental Background-Oriented Schlieren (BOS) imaging data obtained from the Institute of Internal Combustion Engines (IFKM) [26]. The BOS technique provides detailed visualization of the transient hydrogen jet evolution and enables direct comparison of the spatial development of the injected jet with numerical predictions. The primary validation parameter was the macroscopic jet penetration length, as it represents the combined effects of injection momentum, compressibility, and entrainment of the surrounding gas during hydrogen injection. For the numerical analysis, penetration length was defined as the axial location containing 90% of the injected hydrogen mass. Simulated penetration lengths were compared with experimentally derived BOS values at injection pressures of 12 bar and 15 bar. As shown in Figure 2, the numerical results show good agreement with the experimental observations, reproducing both the transient jet development and the dependence of penetration behavior on injection pressure. The agreement is strongest in the near and intermediate jet regions, with larger deviation observed downstream.

This is associated with increasing dispersion of the hydrogen jet and enhanced mixing with the surrounding gas, which weakens density gradients and increases uncertainty in jet-boundary determination. In the BOS measurements, penetration length is derived from density-gradient variations in the optical field, whereas the numerical analysis determines it from the hydrogen mass distribution; some divergence between the two approaches is

https://doi.org/10.3390/hydrogen7030123

therefore expected, particularly where hydrogen concentration becomes highly diluted. As shown in Figure 2, the deviation between simulation and experiment remains within approximately 5–15% up to a penetration distance of approximately 25 mm, increasing gradually to approximately 20–22% at the maximum measured penetration length. This increase is mainly attributed to the higher sensitivity of BOS-based jet-boundary detection in low-density-gradient regions, where small variations in the optical signal produce larger uncertainties in the extracted jet contour. In addition to macroscopic penetration behavior, the numerical framework was qualitatively compared against localized compressible flow structures, particularly Mach disk formation, which occur under highly under-expanded conditions when high-pressure hydrogen expands into a lower-pressure ambient environment. As shown in Figure 3, both the experimental BOS images and numerical predictions exhibit visually comparable barrel shock structures. At high pressure ratios ($p/p_0 \approx 6.7$), distinct Mach disks are observed, indicating supersonic jet flow; with decreasing pressure ratio, the shock structures become progressively weaker and eventually disappear, consistent with the trend reported in [27]. However, the fine-scale shock behavior—including precise Mach disk location, diameter, and barrel shock geometry—has not been captured with sufficient accuracy in the present study. This is attributed to the limited spatial resolution of the BOS imaging technique relative to the shock-cell length scales involved, as well as the need for a more detailed, dedicated shock-capturing numerical setup (e.g., finer near-field mesh resolution and a compressibility-corrected turbulence treatment) beyond the scope of the present framework. Accordingly, this comparison is presented as qualitative only and does not constitute a quantitative validation of Mach disk location or barrel-shock geometry.

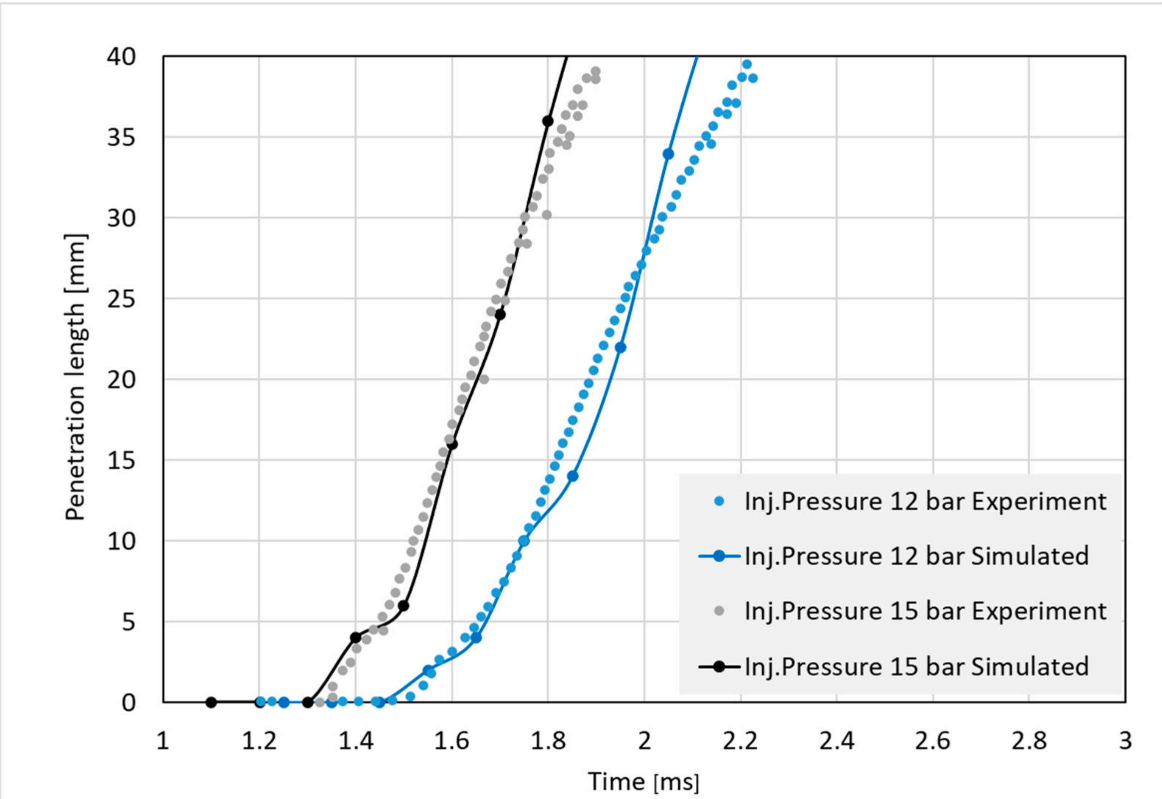

Figure 2. Comparison between experimental BOS data and CFD simulation for hydrogen spray penetration at 12 bar and 15 bar injection pressures.

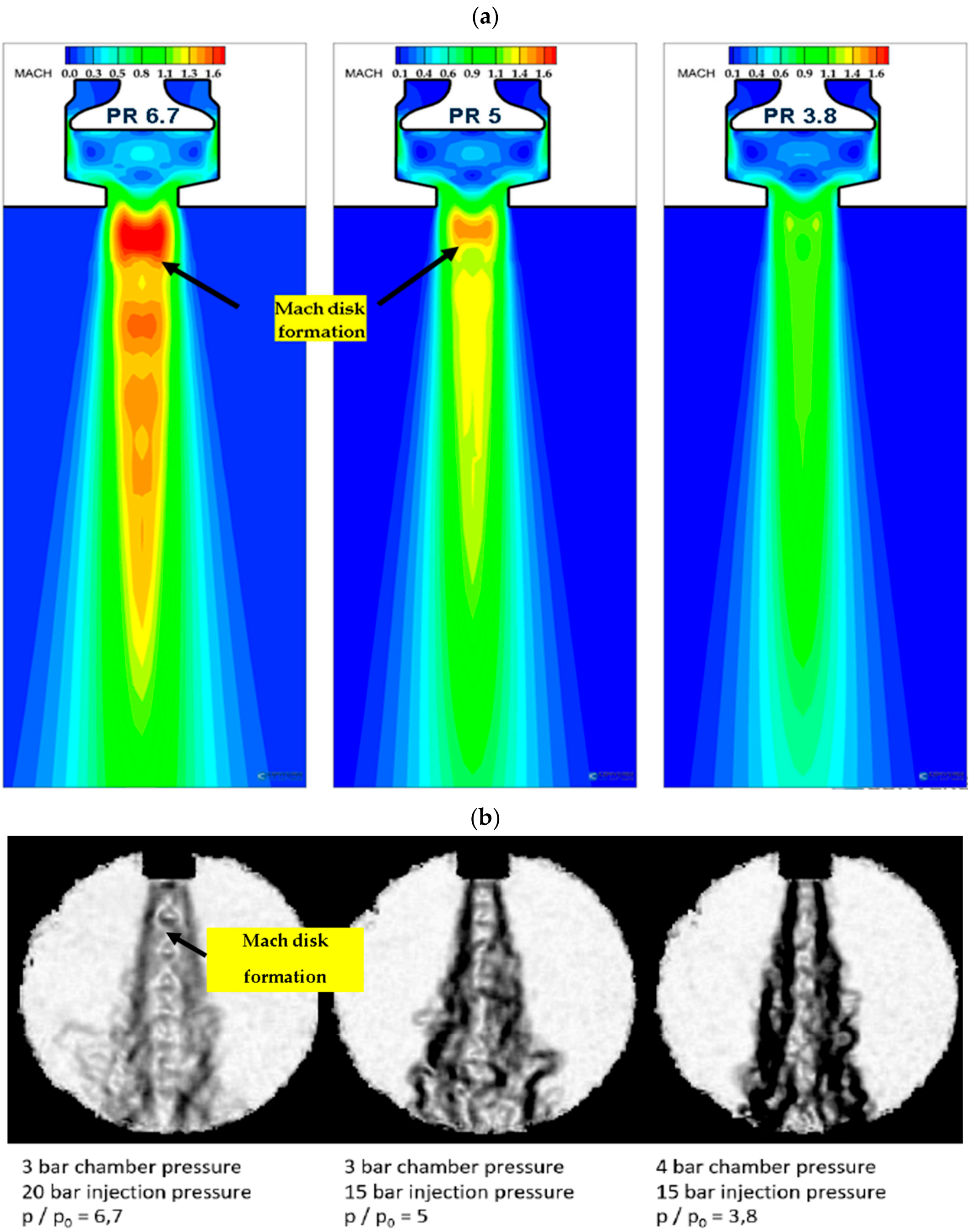

Figure 3. (**a**) Simulated Mach number contours at pressure ratios (p/p0) of 6.7, 5, and 3.8. (**b**) Experimental Background-Oriented Schlieren (BOS) visualizations at matching pressure ratios (PR) [26].

3. Methodology

To ensure the integrity of the comparative analysis, the initial charge motion was maintained identical for all simulation cases. The initial flow field was prescribed with uniform thermodynamic properties and boundary conditions, as summarized in Table 1. The baseline simulation was first performed for two complete engine cycles, starting from the point at which the exhaust valve was half-open. This initialization procedure was adopted to minimize the influence of non-physical transient effects associated with the initial flow field and to ensure that the subsequent simulations were performed under stabilized in-cylinder conditions. The initial species composition was defined according to the relative air–fuel ratio. For the initial condition, the cylinder contents were assigned as a mixture of air and residual exhaust gases, with the corresponding mass fractions adjusted to achieve a relative air–fuel ratio (λ) of 2.5. The turbulence length scale at the inlet boundary was specified as 20% of the inlet diameter, following the standard inlet turbulence initialization approach. The hydrogen injection event was initiated at 570° crank angle (CA) and terminated at 600° CA ash shown in Figure 4. The injection timing was selected to coincide with the intake valve closing (IVC) position, allowing the injected hydrogen jet to interact with a stabilized and fully developed in-cylinder flow field. This approach avoids the influence of highly transient flow structures typically generated during valve motion and enables a more consistent assessment of the effects of injection parameters on hydrogen mixing and combustion behavior.

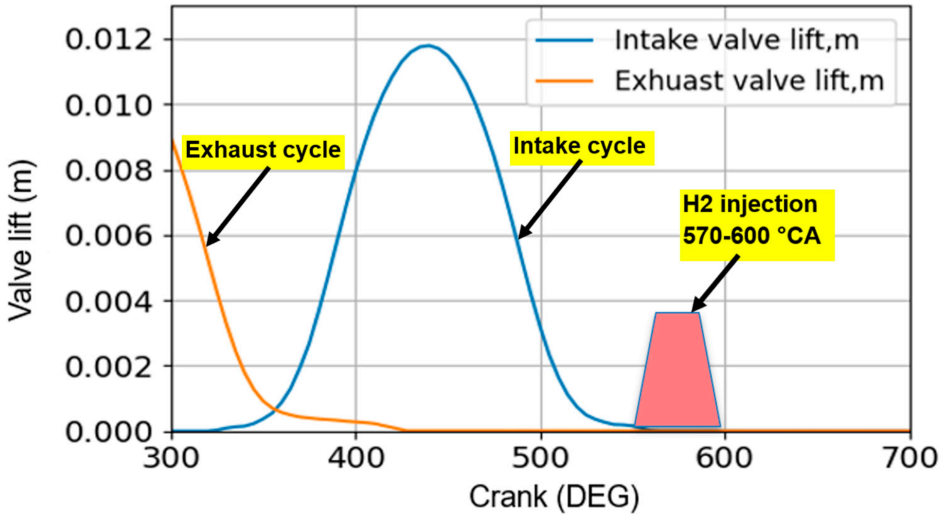

Figure 4. Engine timing diagram showing intake and exhaust valve lift profiles and the specific H2 injection window (570–600 °CA) following intake valve closure.

To capture the interdependencies between nozzle geometry and spray orientation, the simulation results are primarily analysed across two specific cross-sectional planes, as shown in Figure 5. The XZ plane and XY plane serve as the primary observation windows, as they are most critical for characterizing the tumble and swirl motion within the chamber, respectively. These planes are strategically angled to be in line with the injector inclination (for the XZ plane) and the azimuthal rotation (for the XY plane), ensuring that the evolution and penetration of the injected fuel jet remain the central focus of the aerodynamic assessment. The experimental matrix involves four blow cap configurations and five injector rotation angles. Blow cap angles were varied from a baseline vertical injection (WO BK) to deflection angles of 45° (BK45), 65° (BK65), and 75° (BK75) from the vertical axis, as illustrated in Figure 6a. Simultaneously, the injector was rotated at angles of +60° (P60), +30° (P30), 0°, −30° (M30), and −60° (M60), as shown in the plan view in Figure 6b. The complete set of simulated cases is summarized in Table 4. This systematic approach ensures that the subsequent analysis captures the complex interdependencies between nozzle geometry, spray orientation, and the resulting mixture homogeneity.

Table 4. Matrix of simulated test cases representing the various combinations of blow cap geometries and injector rotation angles.

Case Setup	P60	P30	0	M30	M60
BK75	✔	✔	✔	✔	✔
BK65	✔	✔	✔	✔	✔
BK45	✔	✔	✔	✔	✔
WO_BK	NA	NA	−ve z axis	NA	NA

https://doi.org/10.3390/hydrogen7030123

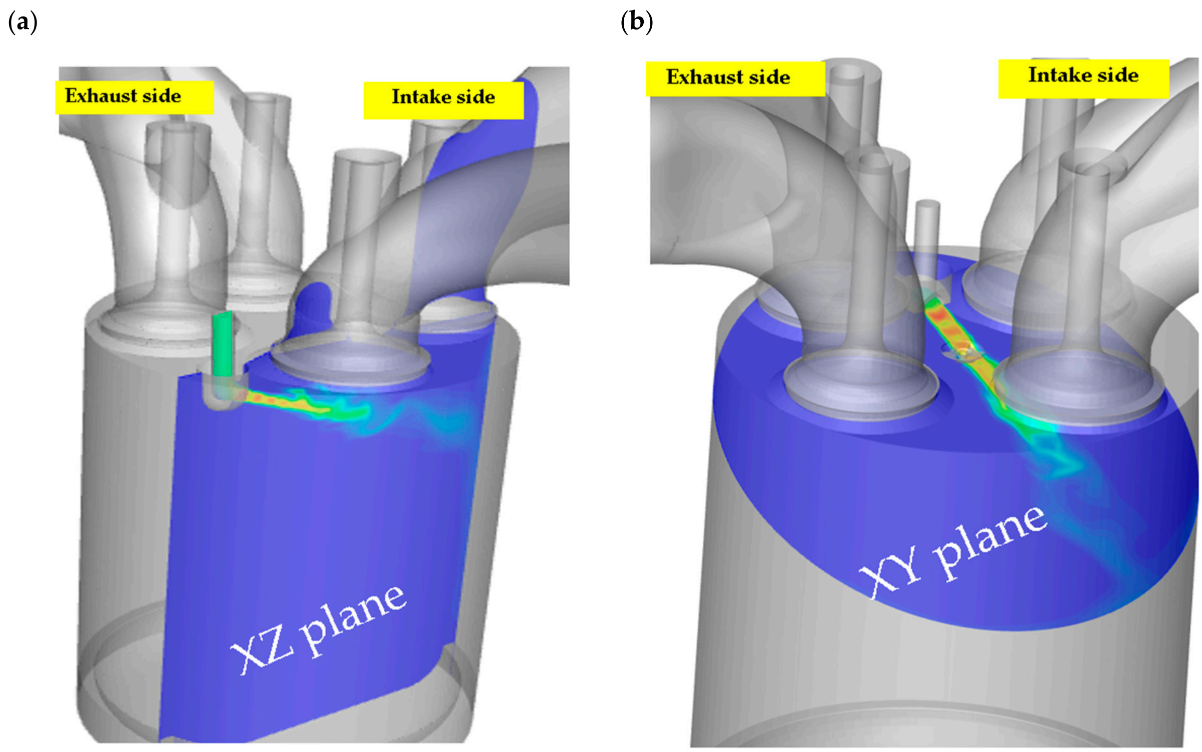

Figure 5. (**a**) Vertical XZ plane aligned with the injector inclination angle for tumble characterization. (**b**) Transverse XY plane aligned with the azimuthal angle for swirl characterization.

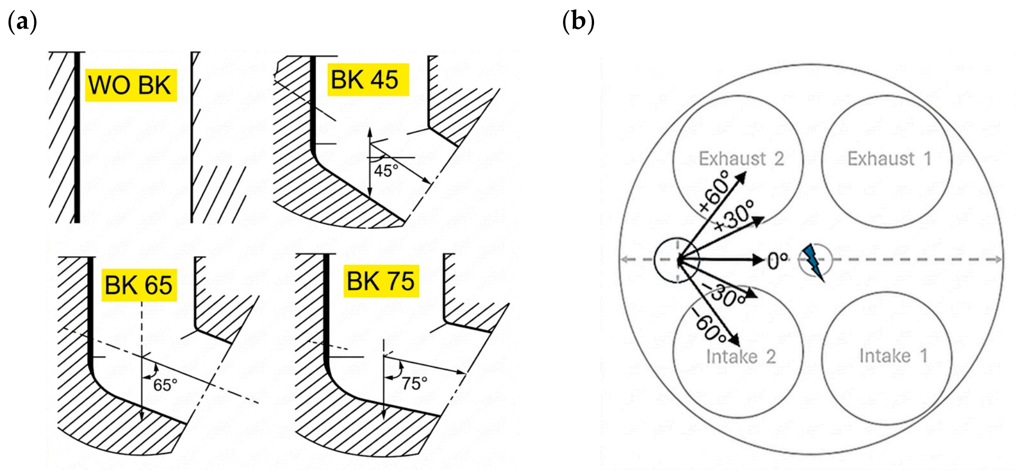

Figure 6. (**a**) Tested blow cap (BK) geometries with deflection angles from vertical. (**b**) Plan view of the injector rotation angles relative to the spark plug and intake/exhaust valves.

4. Results and Discussion

The transition from the intake stroke to the injection phase represents a critical shift in the in-cylinder flow field. While the intake process establishes the baseline charge motion, the subsequent high-pressure direct injection of hydrogen introduces a significant mass and momentum input into the combustion chamber. This injection event does not merely supply fuel; it strongly modifies the pre-existing flow field and charge motion through its high-momentum jet interaction. Because the mixing timescale in hydrogen direct-injection engines is very short, combustion performance and emission characteristics are primarily governed by how this injected momentum is redistributed and dissipated during the early stages of injection. The analysis in this study focuses on geometric parameters that govern this process, particularly injector orientation and blow cap angle, as these define the physical boundary conditions of the in-cylinder flow and remain fixed regardless of operating calibration. These geometric settings provide a hardware-based means of controlling the development of charge motion and mixing behavior. To quantify the resulting aerodynamic behavior, tumble and swirl ratios are used as primary metrics [24]. These dimensionless parameters represent the intensity of organized rotational motion about the horizontal and vertical cylinder axes, respectively, and are commonly used as indicators of in-cylinder charge motion strength. Higher values are generally associated with enhanced mixing due to increased flow organization and momentum transport. However, swirl and tumble ratios represent global, volume-averaged quantities and do not capture local flow structures. Therefore, they are evaluated together with velocity magnitude contours and streamline patterns to accurately resolve differences in flow topology and mixing characteristics.

4.1. Effects of Injection on the Mixing Process

The impact of the high-velocity hydrogen jet on the stabilized intake charge is immediate and transformative. As illustrated in Figure 7, the momentum of the hydrogen jet significantly alters the baseline in-cylinder airflow, transitioning the charge motion from an initially organized state to a strongly disturbed flow field characterized by localized hydrogen-rich regions. This interaction plays a key role in determining the fuel–air mixing process, which in turn influences combustion stability and emission formation. Figure 7a presents the in-cylinder flow field prior to injection, showing a relatively stable, clockwise-oriented velocity structure. With the onset of injection, this flow field is substantially modified, as shown in Figure 7b, where the jet momentum disrupts the existing charge motion and induces a reversal in the dominant flow direction, resulting in a counterclockwise-oriented structure. The mechanism by which the injected momentum is converted into organized in-cylinder charge motion is illustrated through the streamlines in Figure 8. In the XZ plane (a), the vertical component of the hydrogen jet impinges on the cylinder liner and piston head, subsequently curling into a longitudinal vortex structure that generates tumble motion. In the XY plane (b), the lateral deflection of the jet induces rotational motion about the cylinder axis, establishing the swirl profile. This visualization highlights a key aspect of the present study: the development of tumble and swirl structures is strongly governed by the jet trajectory after leaving the nozzle, making the impingement angle on the cylinder liner and piston head a critical parameter in determining in-cylinder charge motion.

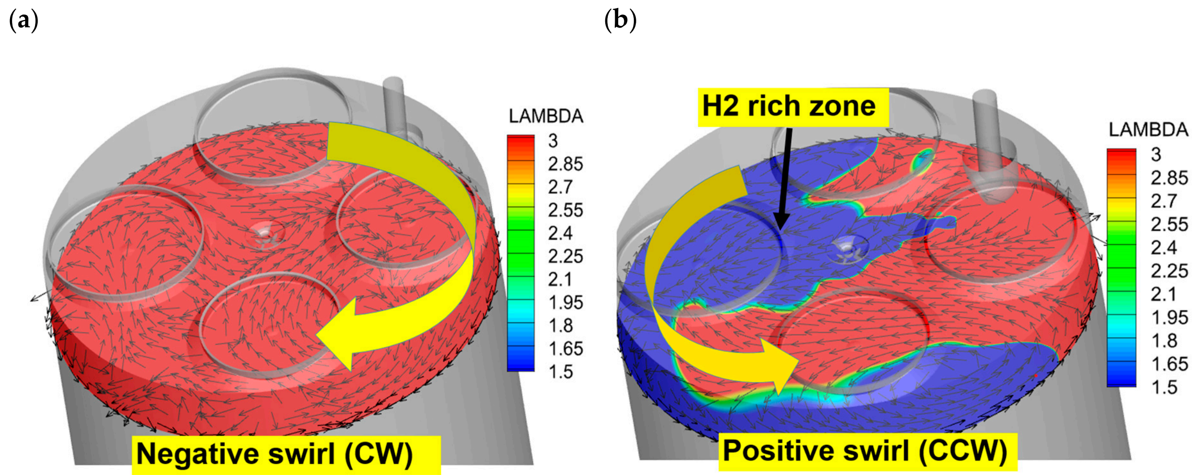

Figure 7. Planar cross-section at the injector outlet: (**a**) pre-injection flow field showing baseline airflow; (**b**) injection phase highlighting H_2-rich zones and jet-induced flow disruption.

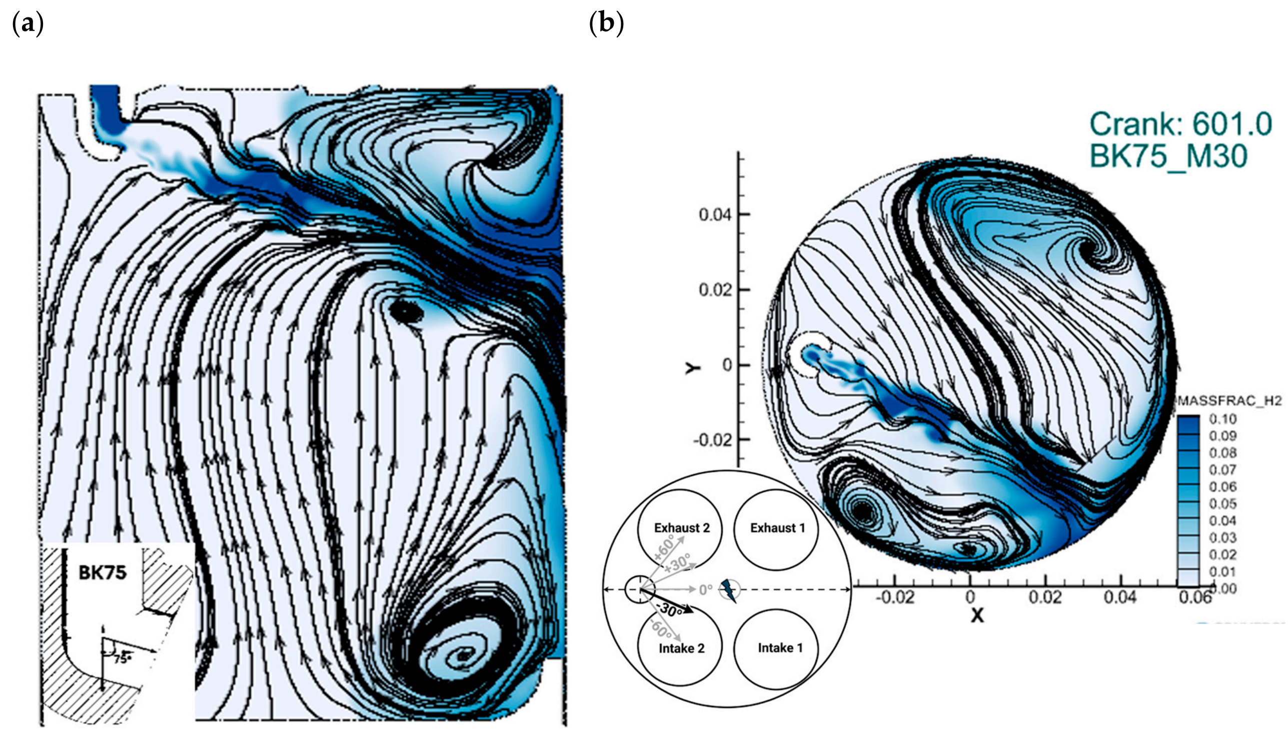

Figure 8. (**a**) Streamline development in the XZ plane showing the conversion of jet momentum into vertical tumble. (**b**) Streamline development in the XY plane showing the formation of horizontal swirl following impingement.

4.2. Blow Cap Inclination Angle Variation

To identify the optimal vertical deflection for hydrogen mixing, a control injector rotation angle of −30 was maintained while varying the blow cap geometry. The analysis first evaluates the macroscopic charge motion through tumble and swirl ratios, as shown in Figure 9. The results reveal a distinct directional bias in tumble generation. In the Y-direction (XZ plane), the WO BK case achieves the highest tumble ratio, followed by BK45, with BK65 and BK75 showing the lowest magnitudes. However, the trend flips with swirl ratio with BK65 and BK75 significantly outperforming BK45 and WO BK. To explain why these specific trends, occur, the following plots and discussions delve into the physical behaviour of the fuel jet.

Firstly, the trend observed in Y-direction tumble generation can be explained simply by the average in-cylinder velocity profiles shown in Figure 10. The WO BK case maintains the highest average velocity throughout the injection event, exceeding 1400 m/s, because a larger portion of the injected mass maintains a velocity close to the initial peak discharge speed of the jet since the distance to impingement is at its maximum. As the blow cap angle increases from BK45 to BK75, the distance between the injector and the impingement surface (the liner and cylinder head) decreases, leading to faster kinetic energy dissipation. This results in progressively lower velocity plateaus during the injection holding phase—approximately 800 m/s for BK45 and 650 m/s for BK75—observed in the velocity profiles. This hierarchy closely mirrors the Y-tumble ratios shown in Figure 9, where WO BK > BK45 > BK65 > BK75. The higher average velocity in the WO BK case sustains a stronger rotational motion about the *Y*-axis; however, the jet largely maintains its coherence and does not undergo significant breakup, leading to delayed fuel dispersion and limited early-stage mixing. In contrast, blow cap configurations promote jet impingement and breakup, enhancing spatial fuel spread and mixing. Among these, BK45 provides the strongest combination of sufficient momentum and effective jet disruption, enabling earlier and more efficient mixture formation. As the impingement distance decreases with increasing blow cap angle, the associated reduction in velocity reflects a loss of kinetic energy required to sustain large-scale tumble structures, which contributes to the systematic decline in Y-direction tumble intensity.

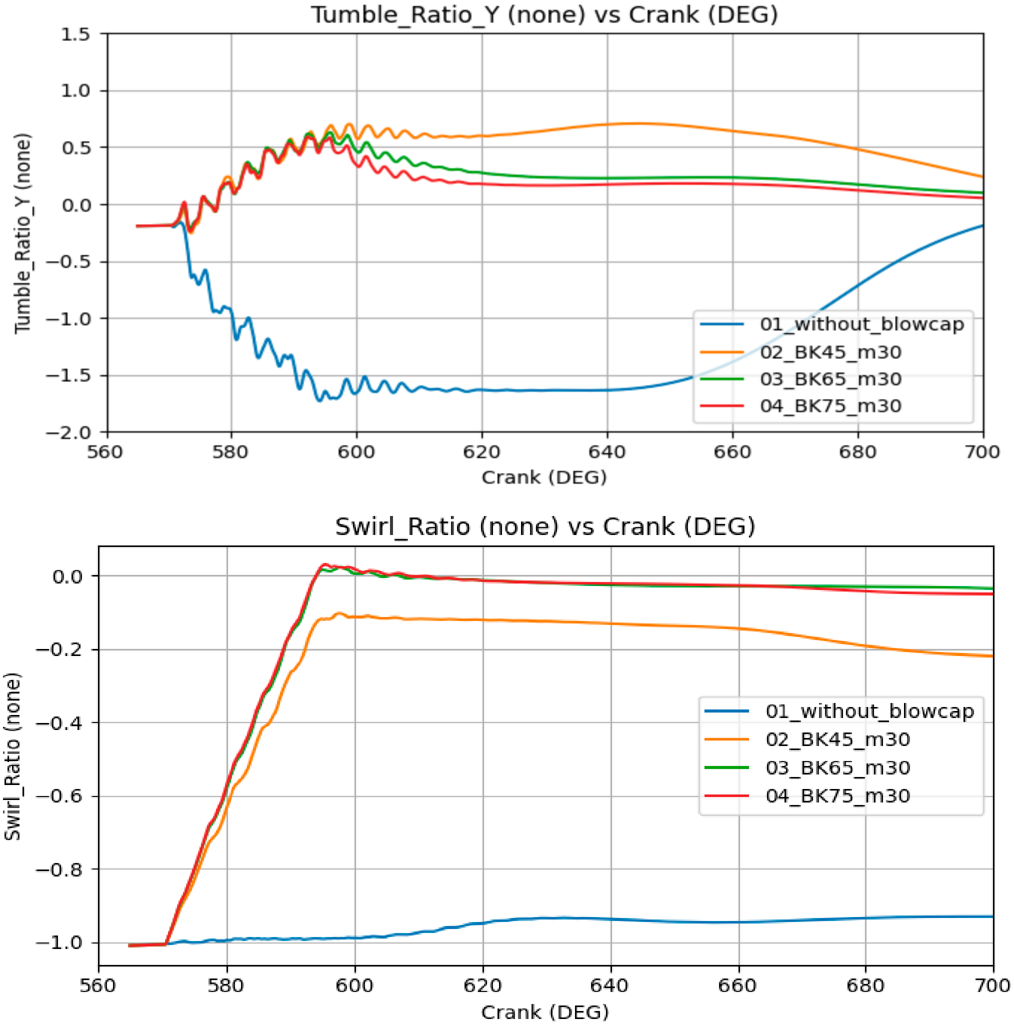

Figure 9. Tumble (XZ plane) and swirl (XY plane) ratio development for different blow cap geometries at a fixed -30° injection angle.

This physical interpretation is further corroborated by the velocity magnitude streamlines presented in Figure 11. In the WO BK case, where the charge is injected directly downward, the streamlines clump together to form a singular, massive longitudinal vortex. This is driven by the Coandă effect acting upon the piston head; rather than rebounding off the piston, the jet's high kinetic energy adheres to the piston's contoured surface, which is specifically designed to guide the flow into an organized, vertical motion. This explains the exceptionally high tumble ratios observed for this configuration. The BK45 configuration exhibits a similar clumping phenomenon, though the primary impingement points shift to the cylinder liner. Here, the relatively shallow angle of impingement allows the Coandă effect to keep the jet attached to the vertical plane of the liner with minimal rebound, effectively draining the flow straight downward and maintaining a tumble-heavy orientation. In contrast, the BK65 and BK75 cases show a distinct shift in flow topology where the streamlines are much less concentrated. In these instances, the energy is shattered into a higher number of vortices that are more spread out. Because these injections are more horizontal, the jet hits the liner at a more perpendicular angle creating a significant amount of fluid rebound. Crucially, once this rebounding fluid spreads horizontally, it catches the lateral curvature of the liner via the Coandă effect. While the vertical configurations (WO BK and BK45) keep the energy trapped in the longitudinal plane to maximize tumble, the BK65 and BK75 cases utilize the increased rebound from their steeper impingement to engage the cylinder's circumference. This explains why, as the injection angle becomes more horizontal, the balance of energy shifts from nearly pure tumble in the WO BK case to a more swirl-dominant profile in the BK65 and BK75 configurations.

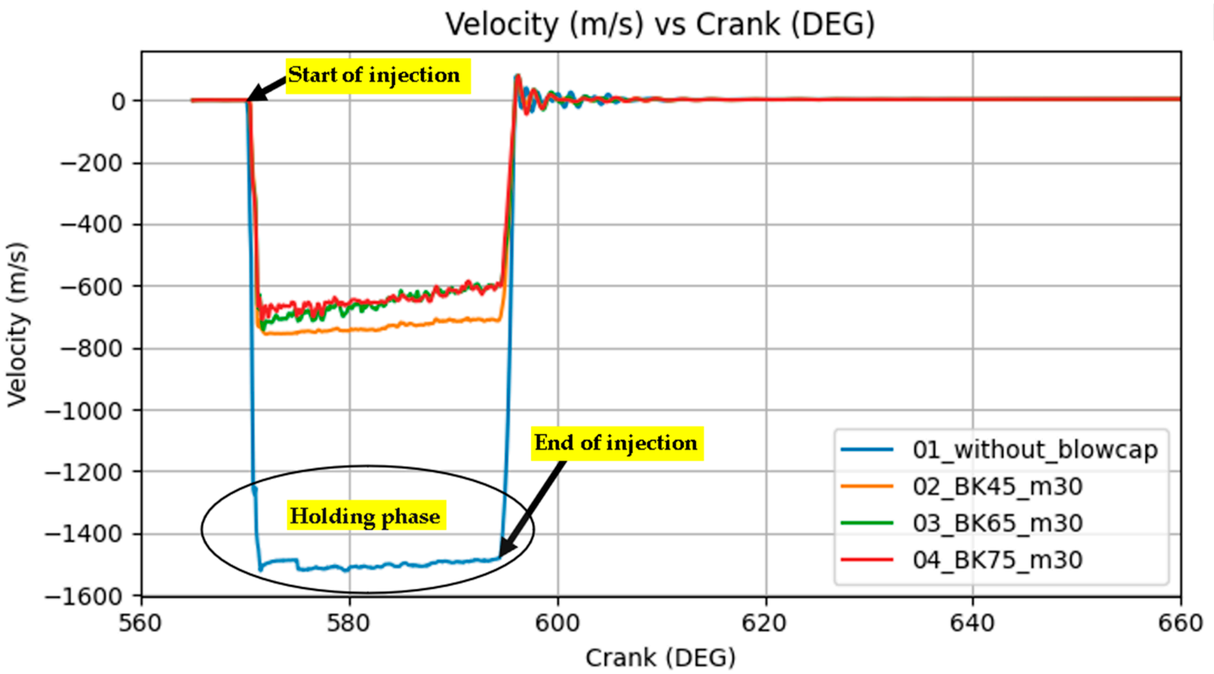

Figure 10. Average charge velocity magnitude vs. crank angle for blow cap inclination angle variations.

While macroscopic ratios provide a baseline, the homogeneity metrics presented in Figure 12 reveal the true effectiveness of each geometry. Despite the high tumble of the BK45 case, the BK65 and BK75 configuration emerges as superior for mixture preparation. This is further supported by the mass fraction distribution bins at 700 CA, where these two cases show the highest frequency of instances near the mean equivalence ratio.

The BK45 and WO BK cases, however, perform poorly in these metrics with BK45 slightly outperforming WO BK. This discrepancy between high-magnitude flow and actual mixing efficiency can be attributed to two primary physical phenomena:

Vortex topology: As evidenced by the streamline plots, the primary driver of homogeneity discrepancy is the structural scale of the vortices. While large-scale, singular vortices (observed in WO BK and BK45) are stable, they act as containment zones that trap the fuel within a longitudinal loop. Conversely, fragmented topologies with multiple smaller vortices act as individual carriers that effectively distribute the charge into stagnant regions (observed in BK65 and BK75).

Balance between primary and secondary flows: Mixture optimization depends on the partitioning of kinetic energy between the secondary flow and the wall-guided primary flow. Direct impingement generates a counter-flow that disrupts the incoming jet to aid mixing, yet excessive rebound energy—as noted in the BK75 case—can still consolidate into a trapping vortex. The superior homogeneity of BK65 is therefore attributed to a balanced energy distribution, where neither the rebound nor the wall-guided flow possesses sufficient energy to form mega-vortices.

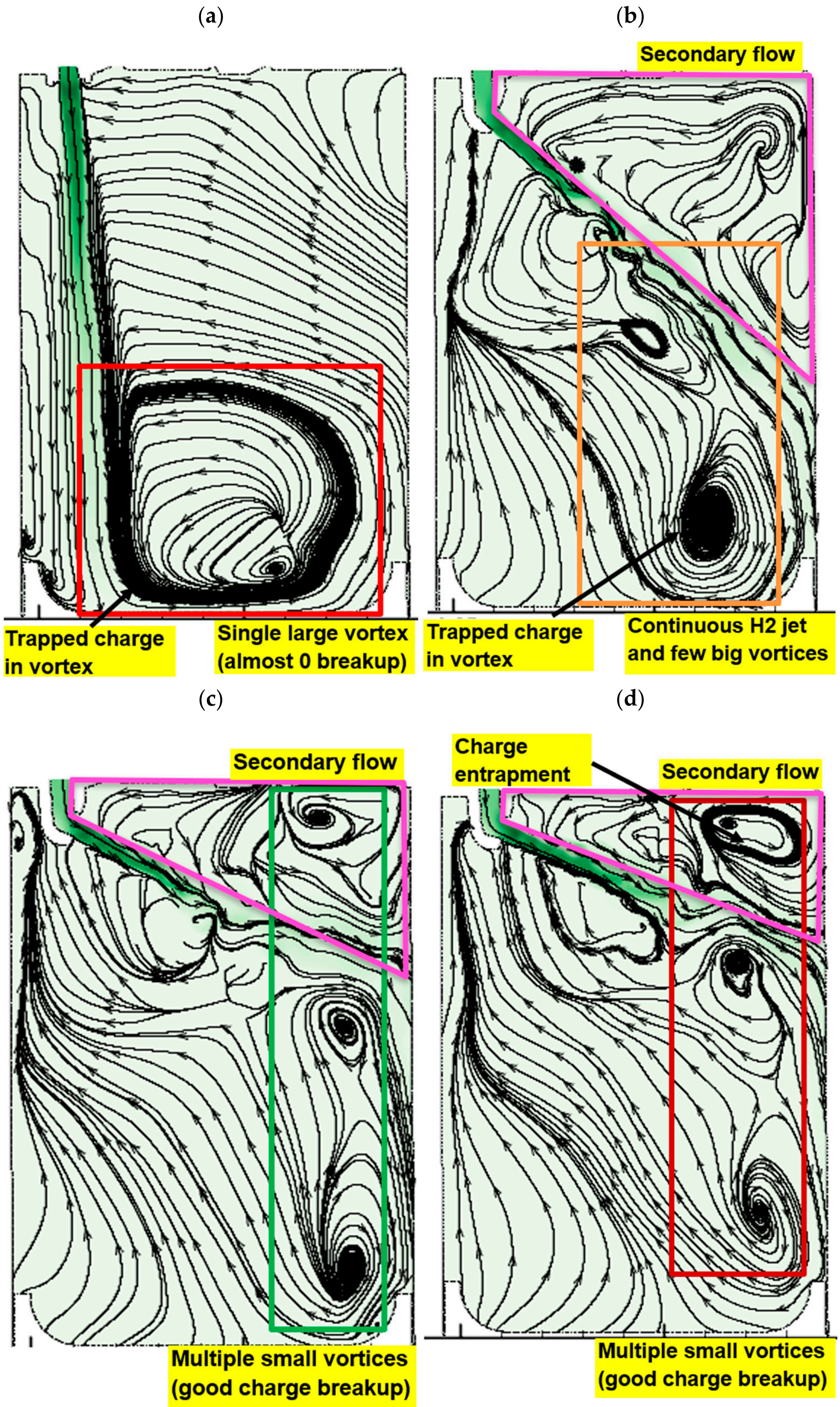

Figure 11. Comparison of velocity magnitude streamlines for the investigated blow cap configurations. (**a**) Without blowcap, (**b**) BK45, (**c**) BK65, (**d**) BK75.

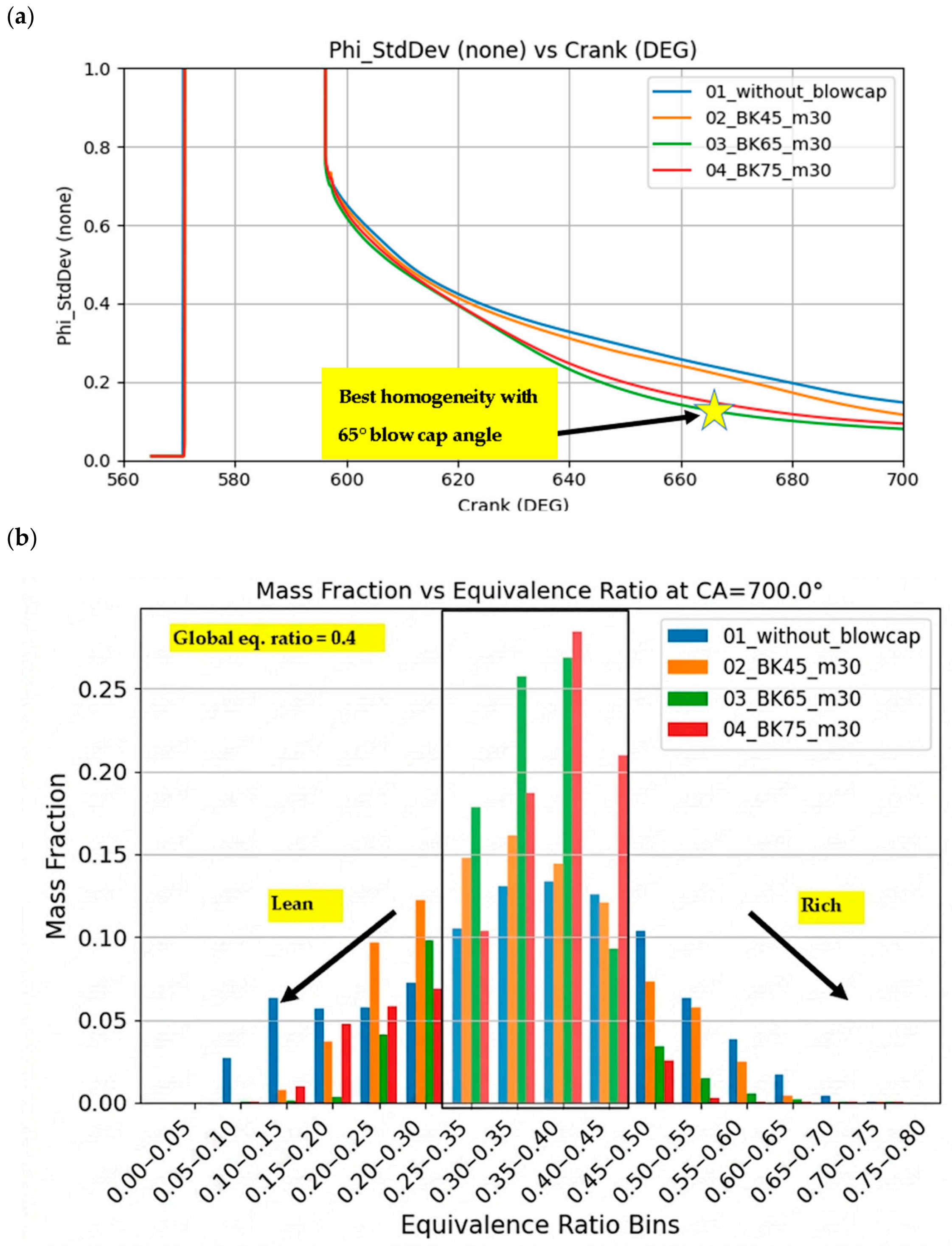

Figure 12. (**a**) Evolution of equivalence ratio standard deviation across crank angles, best case shown with star symbol. (**b**) Mass fraction distribution across equivalence ratio bins at 700 °CA.

4.3. Blow Cap Azimuthal Angle Variation

Having established the BK65 and BK75 blow caps as favorable geometries for promoting jet breakup, the final stage of optimization focuses on the azimuthal orientation of the injector. This subsection evaluates five injector rotation angles ranging from −60° to +60° to assess how the lateral alignment of the fuel jet interacts with the in-cylinder charge motion. Since azimuthal orientation primarily affects the flow in the XY plane, its influence is strongly coupled with the base swirl motion of the engine. As a result, mixture formation is highly dependent on the existing in-cylinder swirl structure. While tumble may develop as a secondary motion due to geometric interaction between the jet and combustion chamber, swirl remains the dominant mechanism governing lateral fuel transport and mixing in this configuration. Therefore, the effectiveness of fuel–air mixing is primarily dictated by the alignment or misalignment between the injected jet and the pre-existing swirl field.

The macroscopic flow analysis illustrated in Figure 13 shows a consistent trend in both tumble and swirl ratios, where absolute magnitudes follow the hierarchy: P60 > P30 > M60 > M30 > 0°. This ordering results from the interaction between the injected hydrogen jet and the pre-existing in-cylinder charge motion. As indicated by the swirl evolution, a dominant clockwise swirl is established during the intake stroke prior to injection, with an initial magnitude of approximately CW 1. Consequently, the positive rotation cases (P30, P60) align the injected jet with the intake-generated swirl motion, as shown in Figure 14a. This alignment reduces jet–flow interaction and promotes momentum conservation, allowing the injected charge to reinforce the existing swirl structure rather than disrupt it. Under these conditions, the jet core remains more coherent, and limited jet breakup is observed due to reduced aerodynamic shear, which restricts early fuel dispersion and mixing. In contrast, the negative rotation cases (M30, M60) orient the injector against the intake-generated swirl, leading to strong jet–swirl interaction within the cylinder. This opposing configuration enhances aerodynamic shear layers at the jet boundary, promoting jet instability and earlier breakup of the core flow. As a result, the hydrogen is more effectively dispersed into the surrounding air motion, improving mixture formation within the combustion chamber. Within each alignment group (P or M cases), the 60° configuration performs better than the 30° case due to differences in jet–wall interaction. At 60°, the shallower impingement angle allows the Coandă effect to dominate, promoting smooth wall attachment and more effective conversion of axial jet momentum into tangential swirl. In contrast, the steeper 30° configuration induces stronger jet rebound from the wall, which weakens the Coandă attachment and disrupts the transfer of axial momentum into organized swirl motion. This mechanical behavior also explains the poor performance of the 0° baseline configuration. As seen in the average velocity profiles in Figure 15, the 0° case exhibits the highest peak velocity (nearly 900 m/s) because, similar to the WO BK configuration in the inclination study, it provides the longest unimpeded jet path before impingement on the liner. This higher undisturbed kinetic energy indicates that the jet maintains its coherence over a longer distance without undergoing significant breakup, resulting in delayed jet fragmentation and, consequently, delayed mixing. However, this high kinetic energy is not effectively utilized after impingement. As shown in the streamlines in Figure 16e, the 0° jet impacts the liner at a near-perpendicular angle, leading to strong flow separation and a pronounced rebound. This results in delayed mixing, as the injected momentum is dissipated into disorganized turbulence rather than being converted into organized charge motion. In contrast, the P and M cases utilize the liner curvature to guide the flow and promote more structured in-cylinder motion, whereas the 0° case exhibits weak conversion of jet momentum into swirl and tumble, resulting in the lowest macroscopic swirl and tumble ratios despite its higher peak velocity.

The homogeneity results in Figure 17 show a trend opposite to that observed for swirl and tumble ratios. Although the P60 case produces the highest swirl and tumble, it results in the worst mixture homogeneity, indicated by a high standard deviation of equivalence ratio. In contrast, the M30 configuration provides the best mixture preparation, followed by the 0° baseline, which shows moderate performance despite weak swirl and tumble generation. This behavior indicates that higher swirl levels in the positive-rotation cases (P30, P60) are not beneficial for mixing. Instead, they promote strong Coandă-driven flow attachment and the formation of large, stable vortical structures. While these structures help preserve momentum, they also trap fuel and restrict its spatial distribution within the combustion chamber, leading to reduced homogeneity. The M30 and M60 cases avoid this behavior by opposing the intake swirl, which increases aerodynamic shear and promotes flow fragmentation. However, in the M60 case, the impingement angle remains relatively shallow, allowing partial vortex formation and limiting full mixing enhancement. In the 0° case, the flow does not exhibit effective or controlled jet breakup; instead, the perpendicular impingement generates two dominant vortical structures on either side of the jet. These vortices assist in fuel transport through vortex-assisted mixing, but the overall flow field remains highly unstructured and does not achieve uniform chamber-wide distribution. Overall, the M30 configuration provides the best balance between maintaining sufficient jet momentum and promoting effective flow fragmentation, resulting in well-distributed vortical structures and the most uniform mixture among all cases.

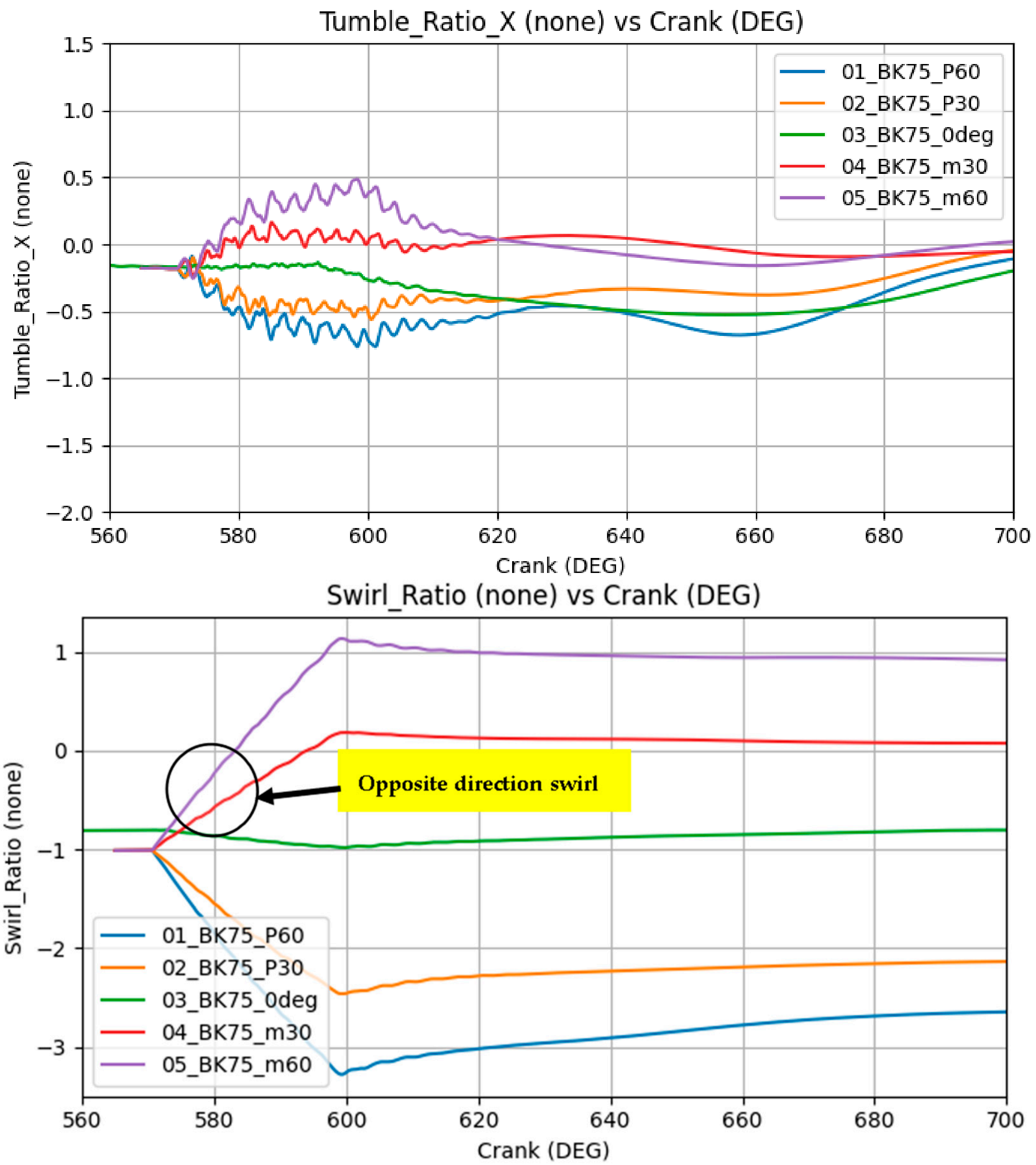

Figure 13. Tumble and swirl ratio development for varying injector rotation angles using the optimized BK75 blow cap.

https://doi.org/10.3390/hydrogen7030123

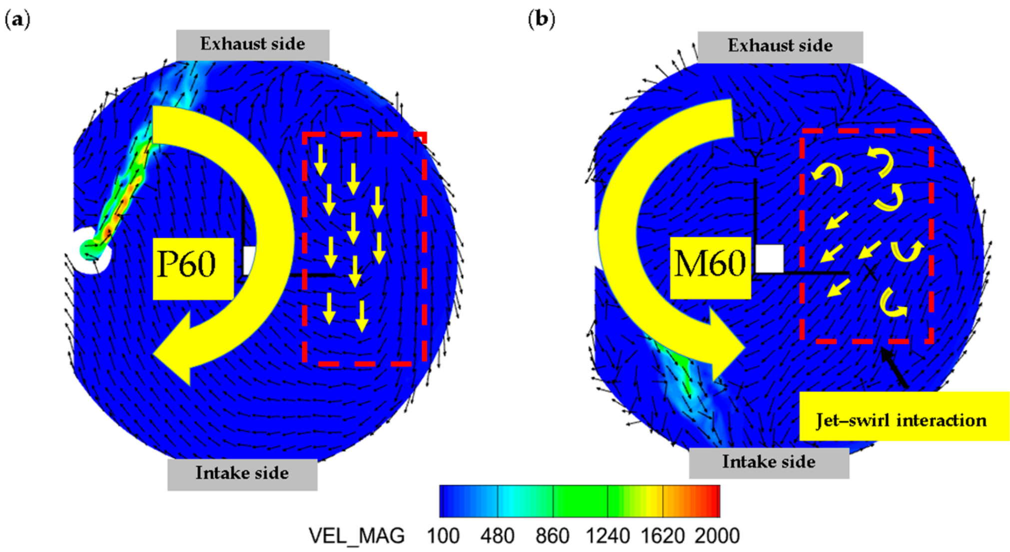

Figure 14. (**a**) P60 orientation showing jet alignment with bulk flow and minimal breakup; (**b**) M60 orientation showing counter-flow interaction and enhanced fuel dispersion.

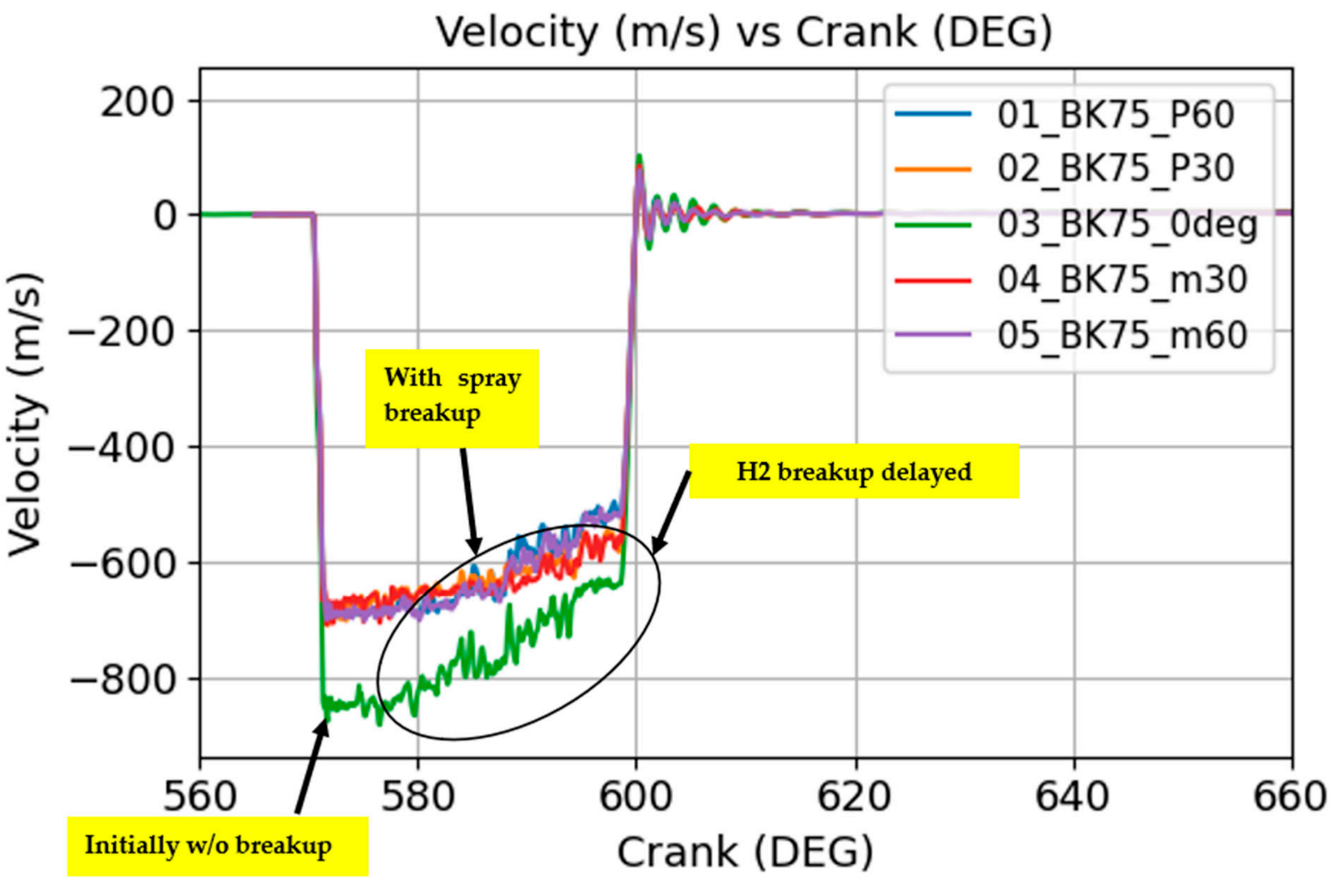

Figure 15. Average charge velocity magnitude vs. crank angle for blow cap azimuthal angle variations.

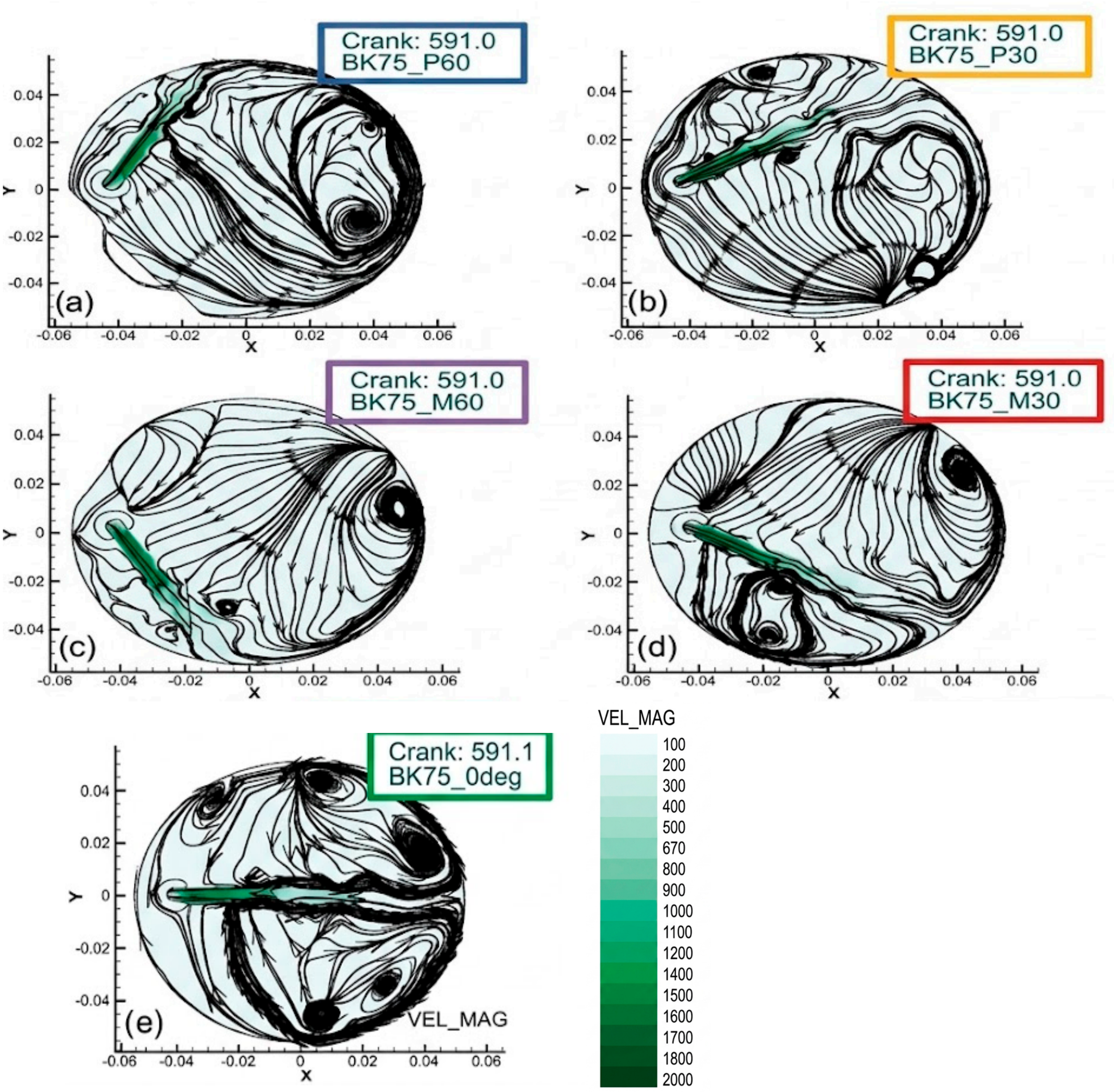

Figure 16. Charge velocity streamlines for azimuthal configurations at 591 °CA: (**a**,**b**) P60 and P30; (**c**,**d**) M60 and M30; (**e**) 0° configuration.

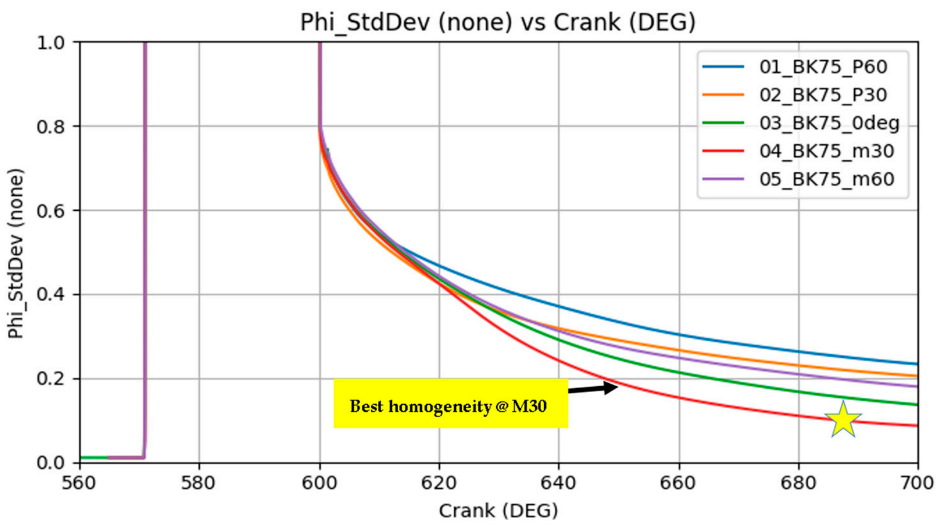

Figure 17. Evolution of equivalence ratio standard deviation for the investigated injector angles, best case indicated with star symbol.

4.4. Selection of Optimal Injector Setup

The internal lambda distributions for the four hardware configurations at the end of the injection process are presented in Figure 18. A comparative assessment of these distributions reveals significant differences in mixture formation, spatial fuel distribution, and local equivalence ratio gradients among the cases.

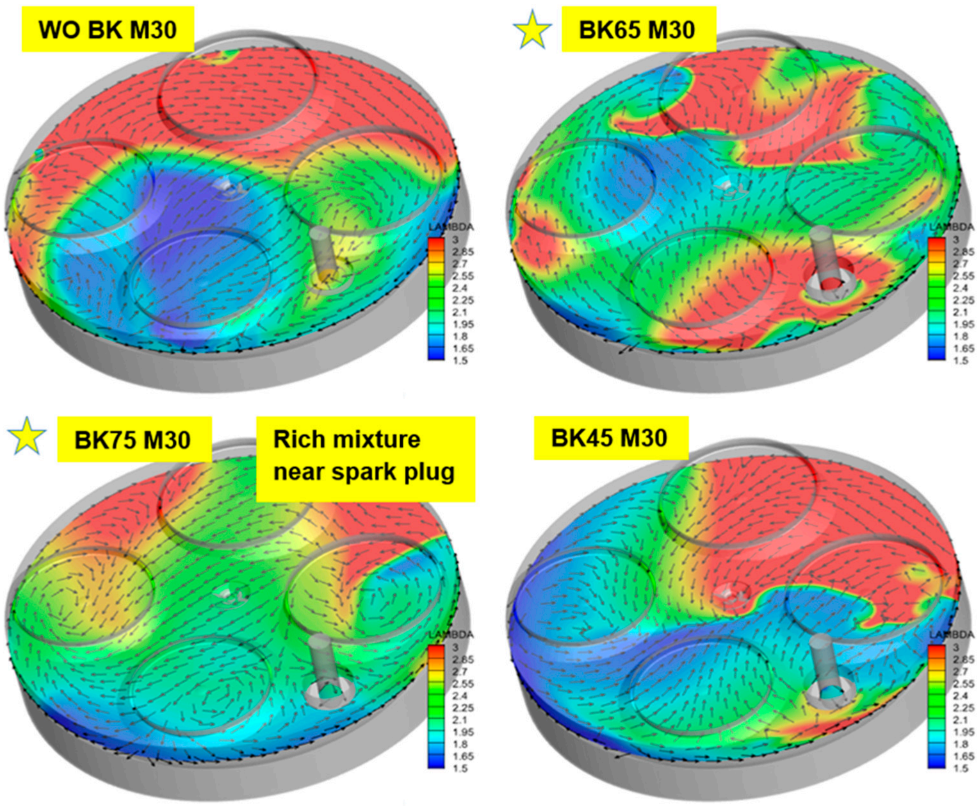

Figure 18. WO BK M30 without blow cap, showing high λ gradients and fuel trapping; BK45 M30, displaying improved but still localized mixing; BK75 M30 and BK65 M30, illustrating the most uniform λ distribution and enhanced mixture homogeneity at 701 °CA, best case indicated with star symbol.

The w/o BK and BK45 M30 configurations exhibit strong non-uniformity in mixture preparation. In the w/o BK case, the injected hydrogen jet retains a coherent structure with limited breakup, resulting in pronounced fuel accumulation and severe trapping within restricted regions of the combustion chamber. This leads to large-scale rich zones and poor spatial redistribution of fuel. In the BK45 M30 configuration, although jet impingement promotes some degree of flow disturbance, the interaction remains insufficient to fully fragment the jet core, leading instead to localized high-concentration regions that are not effectively dispersed by the in-cylinder charge motion. In contrast, the BK75 M30 and BK65 M30 configurations show a clear improvement in mixture homogenization. The increased blow cap deflection promotes stronger jet–wall interaction, enhancing aerodynamic shear and accelerating jet breakup. This results in better fuel dispersion and reduces the formation of isolated rich pockets. Consequently, the overall lambda field becomes more uniform prior to ignition, indicating improved mixing efficiency. Although both high-deflection configurations perform well, the BK65 M30 case demonstrates the most favorable balance between fuel distribution and charge stratification. In this configuration, sufficient local richness is maintained in the vicinity of the spark plug, ensuring reliable ignition conditions, while the remaining chamber volume exhibits a more lean and homogeneous mixture. This combination is particularly beneficial for hydrogen direct-injection combustion, where excessive stratification can lead to combustion instability, while overly lean regions may cause misfire or incomplete flame propagation.

5. Conclusions

This study investigates mixture formation in a direct-injection hydrogen engine, shifting the focus from global flow metrics (tumble/swirl) to the local physical evolution of the hydrogen jet. Our findings regarding injector geometry and jet–wall interaction are summarized as follows:

- Jet Dominance: High-pressure, under-expanded hydrogen injection immediately overpowers pre-existing in-cylinder flow, making mixture formation highly dependent on the jet's post-nozzle trajectory.
- Coandă-Driven Wall Attachment: Low-deflection configurations (BK45) promote Coandă-driven attachment, forming a coherent longitudinal vortex that traps fuel. Higher-deflection cases (BK75) trigger early impingement and flow separation, breaking the attachment to enhance turbulence and mixture homogeneity.
- Swirl Interaction: Injector rotation that aligns the jet with intake-generated swirl (P30, P60) conserves kinetic energy but results in poor homogeneity. Conversely, opposing rotation (M30, M60) induces aerodynamic shear, fragmenting the flow into smaller, well-mixed vortices.
- Hardware Optimization: Wall-guided designs (WO BK, BK45) promote fuel trapping, while excessive rebound (BK75) risks reforming trapping structures. The BK65 M30 configuration provides the optimal balance: it avoids centralized vortex formation to improve global homogeneity while maintaining a locally rich region near the spark plug to facilitate ignition.

Overall, the results demonstrate that injector geometry and orientation strongly influence hydrogen jet–wall interaction, vortex evolution, and local air–fuel distribution. The validated jet penetration results obtained from BOS measurements provide confidence in the predicted macroscopic injection behaviour; however, the available BOS resolution does not allow detailed quantitative validation of the internal shock structures of the highly under-expanded hydrogen jet. Future work will therefore focus on high-resolution Schlieren measurements to characterize and quantitatively validate the Mach disk and associated shock structures, providing further insight into their influence on jet development and subsequent mixture formation.

Author Contributions: B.K.: Writing—original draft, Software, Visualization, Investigation, Formal analysis, Conceptualization. K.K.: Writing and editing, U.W.: Writing—review and editing, Supervision. T.K.: Writing—review and editing, Supervision. All authors have read and agreed to the published version of the manuscript.

Funding: This research was funded by the Federal Ministry for Economic Affairs and Energy, grant number 19I24003F. Open access funding was provided by the Karlsruhe Institute of Technology (KIT) through the Institutional Open Access Program (IOAP) of the Helmholtz Association.

Data Availability Statement: The data presented in this study are openly available in the article.

Acknowledgments: The authors express their gratitude to the Federal Ministry for Economic Affairs and Energy for funding this work within the project PoWer following a decision of the German Bundestag.

Conflicts of Interest: The authors declare no conflicts of interest.

References

1. The European Green Deal. Available online: https://commission.europa.eu/strategy-and-policy/priorities-2019-2024/european-green-deal_en (accessed on 10 March 2026).
2. Intergovernmental Panel on Climate Change (IPCC). Transport. In *Climate Change 2022—Mitigation of Climate Change*; Cambridge University Press: Cambridge, UK, 2023; pp. 1049–1160. [CrossRef]
3. Hill, N.; Raugei, M.; Pons, A.; Vasileiadis, N.; Ong, H.; Casullo, L. *Environmental Challenges Through the Life Cycle of Battery Electric Vehicles*; Study Policy Department for Structural and Cohesion Policies Directorate-General for Internal Policies PE: Brussels, Belgium, 2023.
4. Albrechtowicz, P. Electric vehicle impact on the environment in terms of the electric energy source—Case study. *Energy Rep.* **2023**, *9*, 3813–3821. [CrossRef]
5. Watabe, A.; Leaver, J. Transitioning to battery electric vehicles in Japan: Impact of promotion policy, battery performance and carbon neutrality on greenhouse gas emissions reduction. *J. Clean. Prod.* **2023**, *430*, 139680. [CrossRef]
6. Kalghatgi, G.; Johansson, B. Gasoline compression ignition approach to efficient, clean and affordable future engines. *Proc. Inst. Mech. Eng. Part D J. Automob. Eng.* **2018**, *232*, 118–138. [CrossRef]
7. Liang, Z.; Xie, F.; Jiang, B.; Li, X.; Su, Y.; Wang, Z. Evaluating the potential of mixture formation methods to achieve efficient combustion and near-zero emissions on a hydrogen direct injection engine. *J. Clean. Prod.* **2024**, *439*, 140930. [CrossRef]
8. Priyam, A. *Hydrogen as an Alternative Fuel for Internal Combustion Engines: A Review*; Elsevier Ltd.: Amsterdam, The Netherlands, 2025. [CrossRef]
9. Ghodbane, H.; Khaldi, F.; Bahloul, D. Hydrogen internal combustion engines: Bridging the gap to zero-emission transportation. *Energy Environ.* **2025**. [CrossRef]
10. Guo, S.; Meng, H.; Zhan, Q.; Ji, C.; Wang, D. In-depth analysis of the key combustion parameters in the hydrogen-fueled Wankel rotary engine. *Int. J. Hydrogen Energy* **2025**, *100*, 58–66. [CrossRef]
11. Zhu, X.-M.; Sun, Z.Y.; Liu, X.-Y. Impacts of hydrogen fraction and equivalence ratio on the explosion characteristics of ethanol/hydrogen mixtures. *Fuel* **2024**, *375*, 132620. [CrossRef]
12. Verhelst, S.; Wallner, T. Hydrogen-fueled internal combustion engines. *Prog. Energy Combust. Sci.* **2009**, *35*, 490–527. [CrossRef]
13. Bauer, C.G.; Forest, T.W. Effect of hydrogen addition on the performance of methane-fueled vehicles. Part I: Effect on S.I. engine performance. *Int. J. Hydrogen Energy* **2001**, *26*, 55–70. [CrossRef]
14. Verhelst, S. Recent progress in the use of hydrogen as a fuel for internal combustion engines. *Int. J. Hydrogen Energy* **2014**, *39*, 1071–1085. [CrossRef]
15. Sun, Z.; Hong, J.; Zhang, T.; Sun, B.; Yang, B.; Lu, L.; Li, L.; Wu, K. Hydrogen engine operation strategies: Recent progress, industrialization challenges, and perspectives. *Int. J. Hydrogen Energy* **2023**, *48*, 366–392. [CrossRef]
16. Kinkhabwala, B.; Krishna, K.; Reppert, F.; Wagner, U.; Koch, T. An experimental and computational analysis of backfire initiation and propagation in a single-cylinder hydrogen port-fuel-injection engine. *Automot. Engine Technol.* **2025**, *10*, 16. [CrossRef]
17. Gu, H.; Ren, F.; Nakaya, S.; Tsue, M. A comprehensive experimental and numerical study on turbulent jet ignition mechanisms of lean hydrogen mixture using a super-rich pre-chamber combustion. *Combust. Flame* **2025**, *279*, 114286. [CrossRef]
18. Ye, Y.; Gao, W.; Li, Y.; Zhang, P.; Cao, X. Numerical study of the effect of injection timing on the knock combustion in a direct-injection hydrogen engine. *Int. J. Hydrogen Energy* **2020**, *45*, 27904–27919. [CrossRef]
19. Chen, H.; Zhao, K.; Luo, L.; Ma, Z.; Hu, Z.; Li, X.; Qu, P.; Pei, Y.; An, Y.; Gao, Z. A Numerical Simulation of Mixture Formation in a Hydrogen Direct-Injection Internal Combustion Engine. *Appl. Sci.* **2024**, *14*, 11317. [CrossRef]
20. Scarcelli, R.; Wallner, T.; Salazar, V.M.; Kaiser, S.A. Modeling and Experiments on Mixture Formation in a Hydrogen Direct-Injection Research Engine. *SAE Int. J. Engines* **2009**, *2*, 530–541. [CrossRef]
21. Rouleau, L.; Duffour, F.; Walter, B.; Kumar, R.; Nowak, L. Experimental and Numerical Investigation on Hydrogen Internal Combustion Engine. In *SAE Technical Papers*; SAE International: Warrendale, PA, USA, 2021. [CrossRef]
22. Dhongde, A.; Recker, P.; Sankhla, H.; Virnich, L. Advanced Simulation Methodologies for Hydrogen Combustion Engines. *ATZheavy Duty Worldw.* **2021**, *14*, 46–51. [CrossRef]
23. O'Rourke, P.; Amsden, A.A. A Particle Numerical Model for Wall Film Dynamics in Port-Injected Engines. *SAE Trans.* **1996**, *105*, 2000–2013.
24. Kinkhabwala, B.; Wagner, U.; Ziegler, J.; Koch, T. Hydrogen Combustion Engines for Net Zero Heavy-Duty Transportation—Simulation-Driven Analysis of Injection Parameters Influencing Localized Thermal Hotspots. In Proceedings of the 11th International Symposium on Development Methodology, Wiesbaden, Germany, 11–12 November 2025.
25. Babayev, R.; Andersson, A.; Dalmau, A.S.; Im, H.G.; Johansson, B. Computational characterization of hydrogen direct injection and nonpremixed combustion in a compression-ignition engine. *Int. J. Hydrogen Energy* **2021**, *46*, 18678–18696. [CrossRef]

26. Reimer, J.; Bucherer, M.; Pfeil, J.; Koch, T. Analysis of the jet propagation of hydrogen and helium with PFI- and DI-injectors using BOS (Background-Oriented Schlieren). In Proceedings of the 12th Tagung Einspritzung und Kraftstoffe, Dessau, Germany, 10–11 May 2023; pp. 170–181.
27. Dam, N.J.; Rodenburg, M.; Tolboom, R.A.L.; Stoffels, G.G.M.; Huisman-Kleinherenbrink, P.M.; Ter Meulen, J.J. Imaging of an underexpanded nozzle flow by UV laser Rayleigh scattering. *Exp. Fluids* **1998**, *24*, 93–101. [CrossRef]